

Numerical analysis on the sublimation of low-temperature ablator models undergoing shape change in a supersonic wind-tunnel

D. Bianchi^{*†}

**Sapienza University of Rome, Department of Mechanical and Aerospace Engineering
Via Eudossiana 18, 00184, Rome, Italy*

A. Turchi^{*}

**The von Karman Institute for Fluid Dynamics
Chaussée de Waterloo 72, B-1640, Rhode-St-Genèse, Belgium*

[†]Corresponding author: daniele.bianchi@uniroma1.it

Abstract

Ground testing of ablative materials aims at providing critical data on the material behaviour under relevant conditions for the mission. This is normally done in plasma wind tunnel facilities (i.e., ICP torches, arcjets) although the flow velocity is far from being in the hypersonic regime typical of the actual flight. Hence, in order to perform ablative tests with relevant shape change in a hypersonic facility, non-negligible technical challenges have to be faced. To overcome the limitation induced by the reduced total temperature of hypersonic wind tunnels, low-temperature ablators can be used. There is, in fact, a small number of readily available substances that sublime or ablate in a fashion that can be described fairly accurately by theory at temperatures low enough to make them convenient for use at reasonable supersonic Mach numbers in continuous wind tunnels. Here, a numerical procedure based on CFD analysis to support the definition of the hypersonic capsule shape for the subsequent hypersonic/transonic capsule stability test campaign is presented. The first part of the paper is dedicated to a sensitivity analysis to support the capsule final shape and size selection for experimental testing in VKI facilities. Then, a description of the gas-surface-interaction models implemented into the CFD code for low-temperature ablators thermal response with a discussion of the relevant surface reaction thermodynamics and kinetics is presented. The second part is dedicated to the testing of low-temperature ablators models and their validation including coupled shape-change simulations with mesh evolution and a numerical rebuilding of an experimental test performed in a hypersonic wind tunnel with a camphor model.

1. Introduction

Ground testing of ablative materials aims at providing critical data on the material behaviour under relevant conditions for the mission. This is normally done in plasma wind tunnel facilities (i.e., ICP torches, arcjets). In order to reach the necessary total enthalpy in such facilities, the free-stream flow needs to be heated substantially, i.e. a plasma has to be generated while the flow velocity is far from being in the hypersonic regime typical of the actual flight. Hence, although the total enthalpy of the flight can be duplicated in these ground facilities, there still exists a substantial difference in the flow around the test article, which can strongly affect the distribution of recession along the surface, i.e. the shape change. The effects of the shape change induced by the heat shield ablation in hypersonic flight conditions can alter significantly the capsule stability (through the CoG and CoP variation), especially in the transonic regime, therefore they need to be suitably tackled in ground testing before flight. Hence, in order to perform ablative tests with relevant shape change in a hypersonic facility, non-negligible technical challenges have to be faced. In particular: i) subsonic/supersonic plasma wind tunnel tests do not respect the requirement of "hypersonic testing"; ii) hypersonic impulse facilities (e.g., shock tubes) provide extremely-short test durations and, therefore, they are inherently incompatible with the required time-transient recession measurement; iii) blow-down hypersonic wind tunnels (e.g., the VKI H3 facility) provide a reasonable maximum test duration (i.e. about 30 s), but usually their total temperature is too low to trigger ablation of space-relevant ablative materials. To overcome the limitation induced by the reduced total temperature of hypersonic wind tunnels, low-temperature ablators can be used. Ref. [9] gives an overview on the

NUMERICAL ANALYSIS OF LOW-TEMPERATURE ABLATORS IN A SUPERSONIC WIND-TUNNEL

possible low-temperature materials that undergo sublimation in hypersonic wind-tunnel conditions. There is, in fact, a small number of readily available substances that sublimate or ablate in a fashion that can be described fairly accurately by theory at temperatures low enough to make instrumentation and measurements convenient. Foremost among them are dry ice, camphor, and naphthalene. They are easy to handle, and at first sight their range of thermochemical phase change appears to be extremely convenient for use at reasonable supersonic Mach numbers in continuous wind tunnels. Here, a numerical procedure based on CFD analysis to support the definition of the modified post-ablation shape for the supersonic/transonic capsule stability test campaign is presented. The study is performed with state of the art analysis tools developed by Uniroma with specific application to ablative heat shields for atmospheric reentry vehicles.⁷ The first part of the paper is dedicated to a sensitivity analysis to support the capsule final shape and size selection for experimental testing in VKI facilities. Then, a description of the gas-surface-interaction models implemented into the CFD code for low-temperature ablators thermal response and a preliminary analysis of the relevant surface reaction thermodynamics and kinetics is presented. The second part is dedicated to the testing of low-temperature ablators models and their validation including coupled shape-change simulations with mesh evolution and a numerical rebuilding of the experimental tests performed in the hypersonic H-3 wind tunnel, with both naphthalene and camphor.

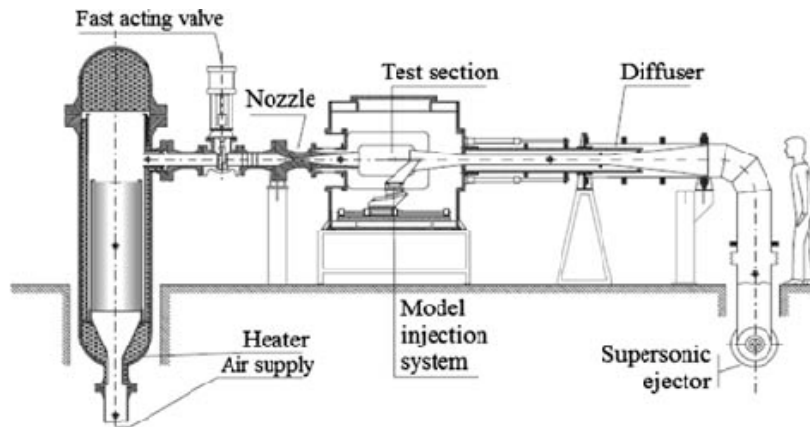


Figure 1: Schematic of the H-3 blow-down hypersonic (Mach 6) wind tunnel.

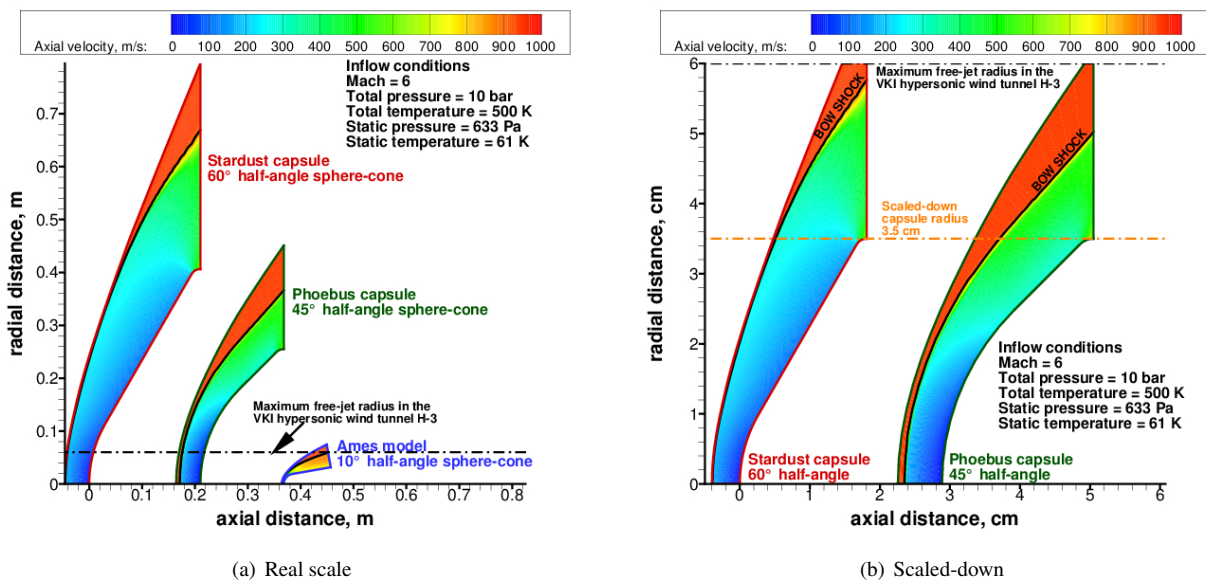


Figure 2: Axial velocity contours for the three selected shapes.

2. Sensitivity Analysis to the Capsule Shape and Size

The ablative boundary conditions have been implemented in a parallel, multi-block, finite volume three-dimensional code that solves the Navier-Stokes equations for compressible single-phase multicomponent reacting systems, including finite-rate chemistry and variable thermodynamic and transport properties. The code, which adopts a standard finite volume Godunov-type formulation, is second order accurate in space uses multi-block structured meshes. The system of equations is approximated by a cell-centered finite volume scheme. The viscous fluxes are approximated by centered differencing, whereas the convective fluxes are computed by means of the solution of a Riemann problem whose left and right states are reconstructed by an interpolation procedure which uses the minmod limiter. The system of ordinary differential equations is advanced in time by means of an explicit Runge-Kutta integration. The flow is assumed to be laminar, in thermal equilibrium, and is modeled with a single-temperature, 6-species (air plus the sublimating gas) and 8-reaction finite-rate chemistry model for air environments. In addition, the code has been parallelized using the OpenMP directives and it can run on SMP computers. The solver has been fully integrated with a customized gas-surface interaction wall boundary condition for carbon-based ablators based on finite-rate heterogeneous surface reactions (including catalytic reactions and surface oxidation, nitridation and sublimation) that allows to calculate the ablation mass blowing flux, the surface chemical composition and the surface temperature as part of the CFD solution. The numerical tool has been validated and verified for pyrolyzing and non-pyrolyzing ablative materials in published works for both external and internal high-temperature flows.^{2-6,8,15}

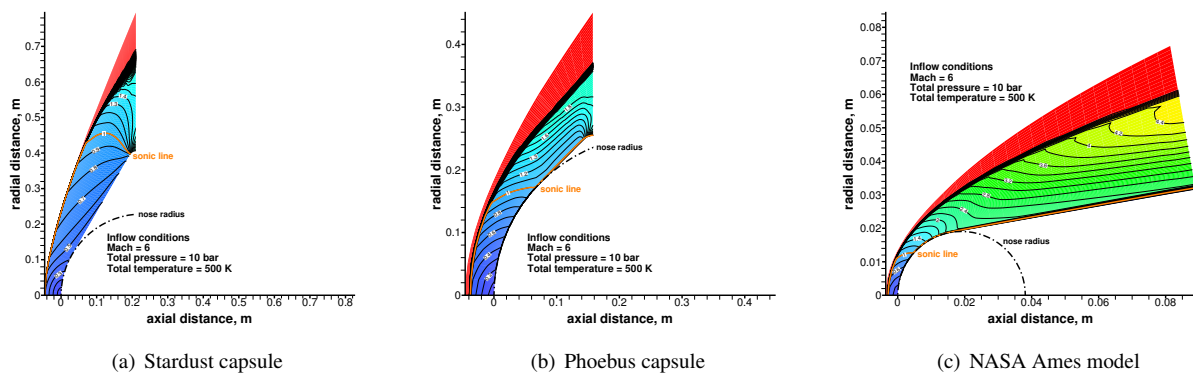


Figure 3: Mach contour and sonic region for different capsules (real scale).

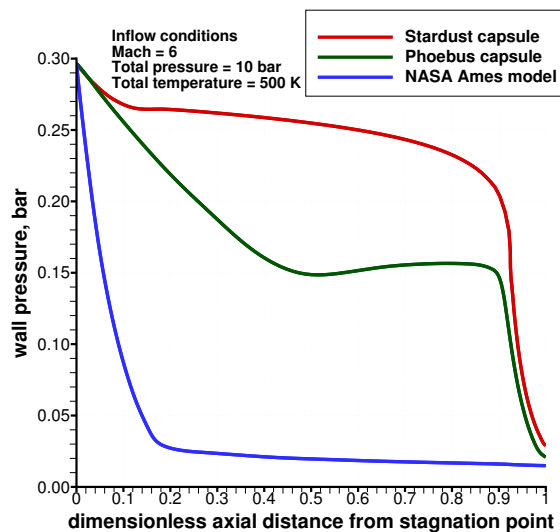


Figure 4: Surface pressure distributions for the three selected shapes (real scale).

Preliminary CFD simulations have been computed to support the capsule shape selection to be tested in VKI

NUMERICAL ANALYSIS OF LOW-TEMPERATURE ABLATORS IN A SUPERSONIC WIND-TUNNEL

facilities. The Mach 6 Hypersonic Wind Tunnel H-3 is the selected facility for the low-temperature ablator experiments undergoing transient heating and shape change, see Fig. 1. The VKI hypersonic tunnel H-3 is a blow-down facility with an axisymmetric nozzle giving a uniform Mach 6 free jet 12 cm in diameter. Air is supplied from a pebble-bed heater at stagnation pressures from 7 to 35 bar and a maximum stagnation temperature of 550 K. Reynolds number may be varied from 3×10^6 to 30×10^6 /m. The test section contains a three-degree-of freedom traversing system for model and/or probe support that also allows the angle of incidence to vary between -35 to $+35$ degrees.

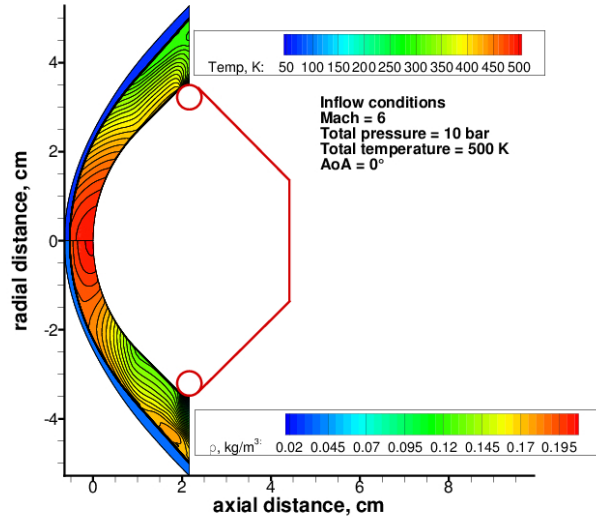


Figure 5: Temperature and density contours for the Phoebus capsule (scaled-down).

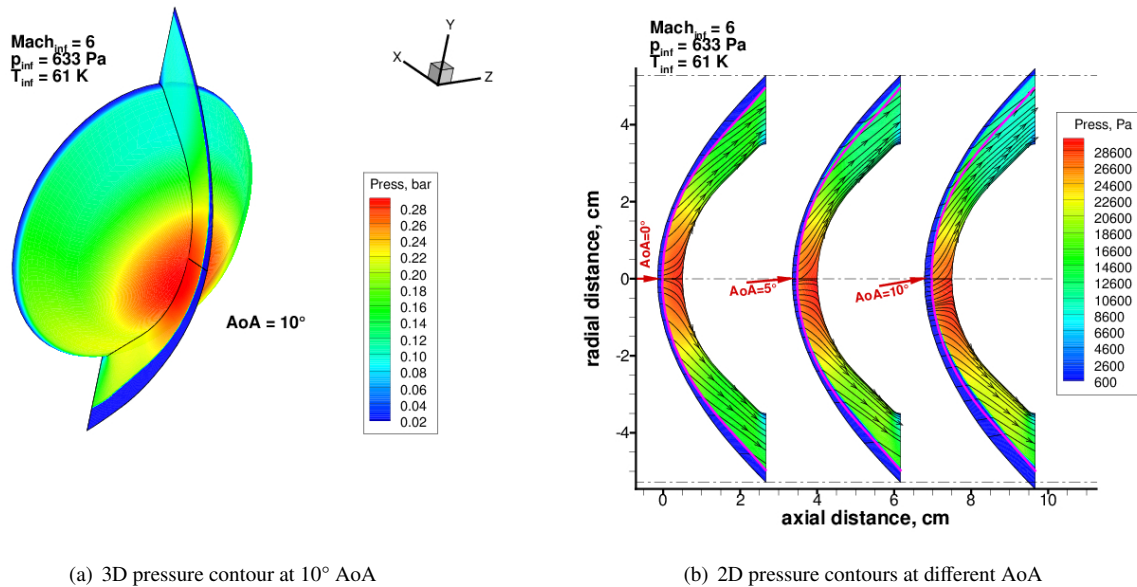


Figure 6: Pressure contour for the Phoebus capsule (scaled-down).

Three different hypersonic capsules have been chosen for this preliminary analysis: i) the Stardust capsule, ii) the Phoebus capsule, and iii) a graphite model that has been tested in the Interaction Heating Facility (IHF) at the NASA Ames Research Center. The three capsules are sphere-cones that are characterized by different nose and shoulder radius and different half-angle. Figure 2(a) shows the three shapes in real scale that have been simulated at a typical hypersonic condition for the H-3 facility (Mach = 6, total temperature = 500 K, total pressure = 10 bar). As shown, both Stardust and Phoebus capsules are significantly larger than the maximum diameter allowed by the H-3 facility. Hence, they need to be scaled down to be tested in the facility. Moreover, larger half-cone angles (i.e. Stardust) produce a larger shock angle than smaller half-cone angles (i.e. Ames model). This further limits the maximum dimension of the capsule

due to the interaction between the shock produced by the capsule itself and the downstream diffuser. If the shock is not entirely captured by the downstream diffuser the wind tunnel cannot be operated in a steady and stable manner. Therefore, the capsule final shape is a trade-off between the available internal space for the instrumentation of balances, that increases with the half-cone angle, and the bow-shock angle, that increases as well with the half-cone angle. The Phoebus capsule is the one that gives a sufficiently large volume to accommodate the balances for aerodynamic force measurements and at the same time a limited bow-shock angle to assure a stable wind tunnel operation. Figure 2(b) shows the results of scaled-down Stardust and Phoebus capsule with a maximum diameter of 7 cm. As it can be seen, for the scaled-down Stardust capsule the bow-shock angle is much wider.

Figures 3(a), 3(b) and 3(c) show the Mach number contours for the three capsules (their real scales have been used). The Ames model is characterized by a small subsonic region that is limited to the first half of the 80° spherical nose. The Phoebus capsule is characterized by a larger subsonic region that extends over the entire 45° spherical nose. The Stardust capsule has a very large subsonic region that extends over the 30° spherical nose and the entire conical part up to the shoulder where, due to the rapid expansion and acceleration, the subsonic flow turns to supersonic. This extended subsonic region that characterizes the stardust capsule is due to the low Mach number of the H-3 facility. In fact, the Mach number of the Stardust capsule in the real re-entry conditions is $\text{Mach} \approx 35$ at peak heating which generates a completely different flow in the conical region, i.e. supersonic and non-uniform. Differently, the large subsonic region produces a region of almost uniform flow as can be better seen by looking at Fig. 4. Such a uniform flow region produces also a rather constant heat flux and consequently a rather constant ablation mass flux, hence reducing significantly the shape change effect that is one of the goals of this activity. For this reason, the Stardust capsule in H-3 flow conditions has been deemed not representative of the realistic flight conditions and associated shape change effects. The Ames model, on the other hand, produces a quite limited subsonic region and a rather extended supersonic and uniform region downstream. The heat flux, as the wall pressure, is strongly varying in the subsonic region and is then weakly changing in the uniform supersonic region downstream. Strong shape change effects are hence expected only in the spherical part but not in the conical part. The Phoebus capsule, finally, appears to be the best solution in terms of pressure and heat flux distributions along the surface with a pronounced wall pressure variation in the first half of the capsule, that is expected to produce a visible shape change effect. Hence, the Phoebus capsule appears to be the best trade-off in terms of volume available for the instrumentation of balances, reduced bow-shock angle for stable wind tunnel operations, and non-uniform pressure and heat flux distributions along the surface to highlight shape change effects. Figure 5 shows the temperature (top) and density (bottom) contours for the scaled-down (7 cm diameter) Phoebus capsule along with the shape and volume of its backshell. The maximum static temperature is ≈ 500 K (corresponding to the total temperature of the flow) and the maximum flow density is ≈ 0.2 kg/m³ at the stagnation point. Further preliminary numerical simulations have been performed on the Phoebus capsule to analyze the effect of the angle of attack and the effect of the scale on the resulting flowfield.

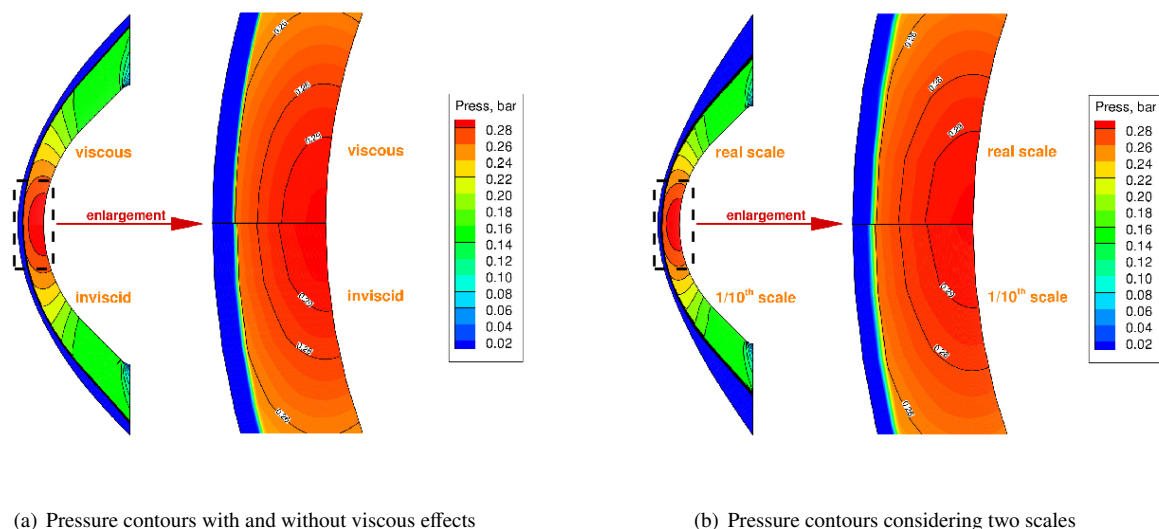


Figure 7: Pressure contours for the Phoebus capsule including viscous and scale effects.

Three-dimensional simulations on the scaled-down (7 cm diameter) Phoebus capsule have been also performed to study the effect of the angle of attack (values of 0° , 5° , and 10° have been considered, compatibly with the wind

NUMERICAL ANALYSIS OF LOW-TEMPERATURE ABLATORS IN A SUPERSONIC WIND-TUNNEL

tunnel operational range) on the bow-shock angle, to avoid the risk of wind tunnel shut-down when the shock travels outside of the downstream diffuser. Figure 6(a) shows the 3D pressure contour for the scaled-down Phobos capsule at 10° AoA. As it can be seen, the bow-shock angle variation is relatively limited. The effect of the angle of attack on the bow-shock angle variation is more clearly visible in Fig. 6(b) that confirms a modest deformation of the bow-shock shape.

Finally, the effect of the scale has been analyzed, including viscous and reacting effects (if any). Numerical simulations have been performed including a 5 species and 8-reaction finite-rate chemistry model for air environment (Park '94) showing null differences between reacting and non-reacting solutions. For the analyzed conditions, in fact, the shock-layer temperature is of the order of 500 K and the shock-layer pressure is of the order of 0.25 bar in the stagnation region, that results in no dissociation of either nitrogen or oxygen. Hence, since chemical reactions are not affecting the results, inviscid solution are not affected by the capsule shape for the considered operational conditions. Viscous effects at different scales are hence analyzed. First, the difference between viscous and inviscid solutions (same scale) on the resulting flowfield is shown in Fig. 7(a). The viscous solution, because of the boundary-layer, increases the shock stand-off distance although the effect is almost indiscernible. Clearly, from Fig. 7(a), the effect of the boundary-layer on the solution and on the shock stand-off distance is negligibly small. Lastly, the difference between real scale and small scale solutions on the resulting (viscous) flowfield is shown in Fig. 7(b). The small-scale solution, because of the smaller Reynolds number, increases the shock stand-off distance although, as for the previous comparison, the effect is almost indiscernible. In conclusion, for the analyzed operational conditions of H-3 facility, finite-rate kinetics effects are null, and scale/viscous effects on the bow-shock shape and stand-off distance are negligibly small. The angle of attack is the only parameter that can practically affect the shock shape and position.

3. Boundary Conditions for Low-Temperature Ablators

In this section, we illustrate the CFD code capabilities for the simulations of a low-temperature ablator (naphthalene or camphor) undergoing spatially varying heating and sublimation and shape change. In order to perform these simulations, an ablation boundary condition for naphthalene and for camphor is implemented into the finite volume Navier-Stokes Solver. This allows simulation of the shape change and the prediction of the correct wall state (temperature, composition and mass loss rate) due to the sublimation process. Often CFD solutions are computed without taking into account either the ablation process or the conduction into the solid. In those cases the mass loss is extrapolated basing on a mass transfer / heat flux analogy with several empirical factors. Hence, it is important to stress that the present results are based on first-principles calculations with no adjustable constants. Here, the gas-solid phase coupling is handled through a customized gas-surface interaction wall boundary condition that has been fully integrated within the CFD solver. The ablating material surface represents an interface between the gaseous atmospheric products flowing over the sample and the low-temperature ablator material so that the solid and gas-phase boundaries are fully coupled at the interface. The ablating material wall boundary condition is based on mass, species and energy conservation equations as reported in Figs. 8 and 9.

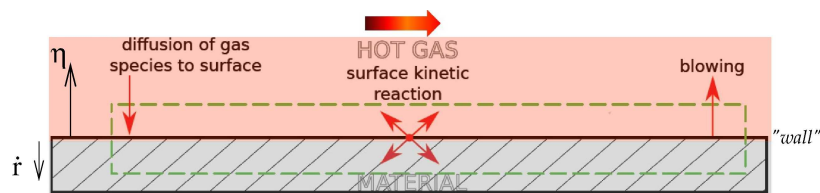


Figure 8: Surface mass balance for an ablating material.

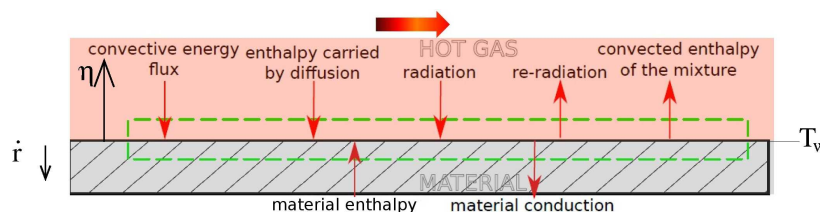


Figure 9: Surface energy balance for an ablating material.

The mass flux of i species (being either atmospheric or ablation product) entering the infinitesimal volume by

diffusion or production by surface reactions must be balanced by the mass flux leaving the volume by convection (see Fig. 8). A proper surface mass balance is hence fundamental to derive the correct amount of mass entering the flowfield from the ablating surface as well as the thermo-chemical boundary layer characterization which will affect the subsequent evolution of the convective fluxes. Convective and radiative heat transfer from the boundary layer, in turn, provide the energy for the thermal decomposition of the surface material, through the surface energy balance (see Fig. 9). The energy flux due to i species entering the infinitesimal volume by diffusion, to material enthalpy and to heat reaching the volume by convection or radiation must be balanced by the energy flux leaving the volume by surface re-radiation, heat conduction within solid and carried away by the produced mass which leaves the surface (blowing of ablative gases). As the surface mass and energy balances are mutually coupled, they must be solved jointly in an iterative way.

The surface mass balance (see Fig. 8) can be written as

$$\underbrace{\rho D \frac{\partial y_i}{\partial \eta}}_{\text{Diffusion}} + \underbrace{\dot{\omega}_i}_{\text{Chemical source}} = \underbrace{(\rho v)_w \cdot y_{i_w}}_{\text{Blowing}} \quad (i = 1, \dots, N) \quad (1)$$

A summation of Eq. (1) over all the species yields the total mass blowing flux

$$\sum_{i=1}^N \dot{\omega}_i = (\rho v)_w \quad \Rightarrow \quad \dot{m}_w = (\rho v)_w = \rho_s \cdot \dot{r} \quad (2)$$

where ρ_s represents the material density and \dot{r} is the surface recession rate.

Multiplying Eq. (1) for each i species's enthalpy and summing over all the species yields an enthalpy balance from mass conservation

$$\underbrace{\sum_{i=1}^N h_i \rho D \frac{\partial y_i}{\partial \eta}}_{\text{Diffusion heating}} + \underbrace{\sum_{i=1}^N h_i \dot{\omega}_i}_{\text{Heat release}} = \underbrace{\dot{m}_w h_w}_{\text{Blowing enthalpy}} \quad (3)$$

The surface energy balance (see Fig. 9) can be written as

$$\underbrace{k \frac{\partial T}{\partial \eta}}_{\text{Convective heating}} + \underbrace{\sum_{i=1}^N h_i \rho D \frac{\partial y_i}{\partial \eta}}_{\text{Enthalpy carried by diffusion}} + \underbrace{\dot{m}_w h_{s,w}}_{\text{Material enthalpy}} + \underbrace{q_{\text{rad,in}}}_{\text{Radiation in}} = \underbrace{q_{c_w}}_{\text{Solid conduction}} + \underbrace{q_{\text{rad,out}}}_{\text{Radiation out}} + \underbrace{(\rho v)_w h_w}_{\text{Blowing}} \quad (4)$$

where h_w represents the enthalpy of the mixture of gases at the surface and $h_{s,w}$ represents the enthalpy of the solid material at the surface temperature.

Substituting Eq. (3) into Eq. (4) and neglecting radiation from the gas-phase (that is a plausible assumption for the present case due to the low total temperature of the flow) yields

$$\underbrace{k \frac{\partial T}{\partial \eta}}_{\text{Convective heating}} - \underbrace{\sum_{i=1}^N h_i \dot{\omega}_i + \dot{m}_w h_{s,w}}_{\text{Heat flux of reaction}} = \underbrace{q_{c_w}}_{\text{Solid conduction}} + \underbrace{q_{\text{rad,out}}}_{\text{Radiation out}} \quad (5)$$

by defining the heat of reaction as $\Delta h_{\text{reac}} = \left[\sum_{i=1}^N h_i (\dot{\omega}_i / \dot{m}_w) - h_{s,w} \right]$ and by assuming steady-state ablation so that the ‘‘heat conduction to solid’’ term can be expressed as $\dot{m}_w (h_{s,w} - h_{s,0})$ with $h_{s,0}$ representing the enthalpy of the solid material at its initial temperature, the final form of the energy balance equation is

$$\underbrace{k \frac{\partial T}{\partial \eta}}_{\text{Convective heating}} = \underbrace{\dot{m}_w \Delta h_{\text{reac}}}_{\text{Heat flux of reaction}} + \underbrace{\dot{m}_w (h_{s,w} - h_{s,0})}_{\text{Solid conduction (steady-state)}} + \underbrace{\sigma \epsilon T_w^4}_{\text{Re-radiation}} \quad (6)$$

where the solid material has been assumed as a grey body with surface emissivity equal to ϵ . Equation (6) can be casted in a different way to highlight the energy balance as follows

$$k \frac{\partial T}{\partial \eta} - \sigma \epsilon T_w^4 = \dot{m}_w (\Delta h_{\text{reac}} + \Delta h_{\text{solid}}) \quad (7)$$

NUMERICAL ANALYSIS OF LOW-TEMPERATURE ABLATORS IN A SUPERSONIC WIND-TUNNEL

where Δh_{solid} is the energy required (per unit of mass) to heat-up the solid material from its initial temperature to the wall temperature and Δh_{reac} is the energy required (per unit of mass) to gasify the solid through different reactions (sublimation, melting, pyrolysis, oxidation, etc.). Hence the amount of mass loss rate is directly proportional to the net heat flux ($k\partial T/\partial\eta - \sigma\epsilon T_w^4$) and inversely proportional to the energy required to gasify the solid phase ($\Delta h_{\text{reac}} + \Delta h_{\text{solid}}$).

For the present case low-temperature sublimating ablators are considered. Hence, the chemical source term, $\dot{\omega}_i$, is zero for the atmospheric species and different from zero for the sublimating species. The sublimation rate is represented by the following equation

$$\dot{\omega}_i = k_j \rho (y_{i,eq} - y_{i,w}) \quad i = \text{sublimating species} \quad (8)$$

where k_j is the effective rate constant for the sublimation reaction j and $\rho y_{i,w}$ is the partial density of species i at wall. The term $y_{i,eq}$ represents the equilibrium mass fraction of the sublimating species i that can be computed from its saturated equilibrium vapor pressure. The effective rate constant k_j can be expressed as

$$k_j = \left(\frac{\hat{v}_j}{4} \right) \cdot \alpha_j \quad (9)$$

where α_j is a constant vaporization coefficient, assumed equal to 0.18 for both naphthalene and camphor¹⁴ (it has been varied between 0.1 and 1 with little difference seen in the result), and \hat{v}_j represents the mean molecular speed of the reacting species

$$\hat{v}_j = \sqrt{8kT_w/\pi m_i} \quad (10)$$

By rearranging the equations, the sublimation rate is consistent with the classical Knudsen-Langmuir equation

$$\dot{\omega}_i = \frac{\alpha_j (p_{i,eq} - p_{i,w})}{\sqrt{2\pi RT_w/M_i}} \quad (11)$$

This expression simply represents a microscopic surface mass balance and requires that the net mass loss rate from the surface, $\dot{\omega}_i$, be the difference between the mass leaving and the mass returning to the surface as represented by the first and second terms in the parentheses on the right-hand side of Eq. (11). Equation (11) adds the equilibrium vapor pressure of the sublimating species, $p_{i,eq}$, as an additional unknown.

Vapor pressure or equilibrium vapor pressure is defined as the pressure exerted by a vapor in thermodynamic equilibrium with its condensed phases (solid or liquid) at a given temperature in a closed system. A model for the vapor pressure of the sublimating sample material has to be adopted in order to compute the chemical source term for the sublimation products. This model is an experimental correlation between temperature and the equilibrium pressure of the pure substance at that specific temperature. In fact, the vapor pressure of a pure substance is only a function of its temperature. Furthermore, the knowledge of the vapor pressure curve and of the melting line permits to draw the phase diagram that represents a useful tool for the prediction of the ablated state of the surface material: for example, the hypersonic wind tunnel conditions, if not properly tuned, can exceed the pure sublimation regime and trigger the liquefaction of the ablating material.

For the special case of a solely sublimating ablator the heat of reaction term becomes a heat of sublimation term and can be expressed as $\Delta h_{\text{subl}} = h_{c,w} - h_{s,w}$, where $h_{c,w}$ is the enthalpy of the sublimating species c at the wall temperature. To close the problem information on the material properties are required. In particular, the enthalpy of the gaseous sublimating species, h_c , the enthalpy of the solid material, h_s , and the equilibrium vapor pressure of the sublimating species, $p_{c,eq}$, are required as a function of temperature. The unknowns of the problem are the chemical composition of the N gaseous species at the wall, $y_{i,w}$, the ablation mass flux, \dot{m}_w , and the wall temperature, T_w . The $N+2$ independent equations that are needed to solve the ablating boundary conditions are

$$\rho D \frac{\partial y_i}{\partial \eta} = \dot{m}_w \cdot y_{i,w} \quad (i \neq c) \quad (12)$$

$$\rho D \frac{\partial y_c}{\partial \eta} = \dot{m}_w (y_{c,w} - 1) \quad (13)$$

$$\dot{m}_w = \alpha \sqrt{\frac{RT_w}{2\pi M_c}} \rho (y_{c,eq} - y_{c,w}) \quad (14)$$

$$k \frac{\partial T}{\partial \eta} - \sigma \epsilon T_w^4 = \dot{m}_w (\Delta h_{\text{subl}} + \Delta h_{\text{solid}}) \quad (15)$$

where

$$\begin{aligned}\Delta h_{\text{subl}} &= (h_{c,w} - h_{s,w}) \\ \Delta h_{\text{solid}} &= (h_{s,w} - h_{s,0})\end{aligned}$$

From a numerical standpoint, the total ablation mass flux, \dot{m}_w , and the wall chemical composition, $y_{i,w}$, are computed from the surface mass balance, Eqs. (12) and (13), coupled with the finite-rate sublimation model, Eq. (14), and using the local pressure and temperature distributions. The wall temperature, T_w , is computed from the surface energy balance, Eq. (15), using an iterative procedure to solve the highly non-linear coupling between the mass and energy balances. At each numerical iteration, the wall temperature, the ablation mass flux, and the wall chemical composition are updated until a steady-state condition is reached. This procedure has permitted to carry out all the computations presented in the next Sections without introducing any further numerical treatment to increase code robustness. Boundary conditions other than an ablating wall are enforced as follows: static temperature, static pressure, Mach number, flow direction and chemical composition at the inflow (supersonic inflow), no assigned conditions at the outflow (supersonic outflow), and symmetry axis.

3.1 Naphthalene model

The material properties required from the model are: i) the enthalpy of the gaseous sublimating species, ii) the enthalpy of the solid material, and iii) the equilibrium vapor pressure of the sublimating species. These three quantities are needed as a function of temperature.

Naphthalene is an organic compound with formula $C_{10}H_8$ with a molecular weight of 128.17052. It is the simplest polycyclic aromatic hydrocarbon, and is a white crystalline solid. The gaseous naphthalene enthalpy and the corresponding specific heat at constant pressure are taken from CEA database while the solid naphthalene was represented with a constant specific heat recovered from NIST. Finally, the value of the standard enthalpy of formation of solid naphthalene is equal to 0.6 MJ/kg. For the transport properties no experimental data have been found and they have been calculated via kinetic theory. Figure 10 shows the naphthalene gas-phase and solid-phase enthalpies along with the heat of sublimation, $\Delta h_{\text{subl}} = h_c - h_s$, as a function of temperature. The standard heat of sublimation at 298.15 K is 0.574 MJ/kg and the heat of sublimation is rather constant over temperature ranging from standard to melting conditions (298.15-353.1 K). Moreover, it is also worth noting that the energy required (per unit of mass) to gasify the solid phase ($\Delta h_{\text{subl}} + \Delta h_{\text{solid}}$) is dominated by the sublimation process, Δh_{subl} , while the energy required to heat-up the solid, Δh_{solid} , can only contribute up to 10% at the highest temperature, i.e. the melting temperature (assuming that the solid is initially at ambient, i.e. standard, conditions). Because of a rather constant heat of sublimation and of the small contribution of the solid heating term, the energy required to gasify naphthalene does not change much with temperature in the sublimation regime.

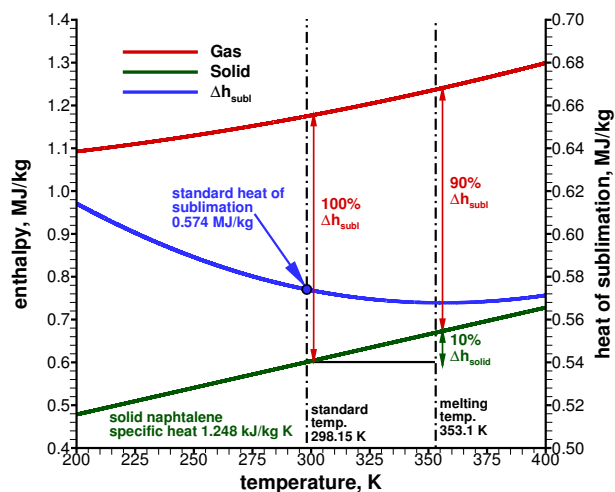


Figure 10: Enthalpy of gaseous and solid naphthalene and Δh_{subl} as a function of temperature.

The remaining information to be retrieved is the naphthalene equilibrium vapor pressure. For the vapor pressure curve of naphthalene two main experimental campaign results have been found in literature and compared (Ref. [13] in

NUMERICAL ANALYSIS OF LOW-TEMPERATURE ABLATORS IN A SUPERSONIC WIND-TUNNEL

the range 313.15-453.15 K and Ref. [11] in the range 280-375 K). Ref. [13] proposes the following Antoine equation that pools author's data with previous works for the sublimation region

$$\log(p) = 10.0896 - 2926.61/(T + 273.772) \quad (16)$$

where the pressure, p , is given in *Torr* and temperature, T , in $^{\circ}\text{C}$. Furthermore, in the article a residual standard deviation of 0.022 *Torr* is reported.

Ref. [11] proposes a different expression for his results

$$R \ln(p/p^{\circ}) = -\Delta G^{\circ}(\theta)/\theta + \Delta H^{\circ}(\theta)(\theta^{-1} - T^{-1}) + \Delta C_p^{\circ}[(\theta/T) - 1 + \ln(T/\theta)] \quad (17)$$

where R is the gas constant, p [Pa] is the vapor pressure, T [K] is the temperature, θ is a reference temperature, ΔG the Gibbs energy of the vapor minus condensed phase at θ , and likewise ΔH° and ΔC_p° (see Fig. 11 for Ref. [11] data).

	θ K	$\frac{\Delta G^{\circ}(\theta)}{\text{J mol}^{-1}}$	$\frac{\Delta H^{\circ}(\theta)}{\text{J mol}^{-1}}$	$\frac{\Delta C_p^{\circ}(\theta)}{\text{J K}^{-1} \text{ mol}^{-1}}$	$\frac{10^2 \langle \delta p^2 \rangle^{1/2}}{p}$
Naphthalene(s) this work	298.15	-5989.4 ± 4	72513 ± 71	-57.53 ± 4	0.8
Naphthalene(s) Ambrose <i>et al.</i> ⁽⁸⁾	298.15	-6010 ± 128	72423 ± 114	-60.7 ± 10	1.6
Naphthalene(l) this work	373.00	-24161 ± 6	50246 ± 150		0.7

Figure 11: Naphthalene vapor pressure parameters from Ref. [11].

In Fig. 12 both expressions have been plotted in the vapor pressure diagram and compared for a typical range of temperature showing negligible differences. Due to the minimal discordance of these experimental curves (with a maximum of roughly 1% in the region of pure sublimation), Ref. [13] is chosen for the implementation in the CFD code for its Antoine expression.

In the phase diagram (Fig. 13) the values of pressure and temperature referring to the triple point are worth to be mentioned. In thermodynamics, the triple point of a substance is the temperature and pressure at which the three phases (gas, liquid, and solid) of that substance coexist in thermodynamic equilibrium. For the naphthalene these values are 353.1 K and 999.87 Pa from Ref. [10]. The vapor pressure of naphthalene increase by roughly two orders of magnitude (from ≈ 10 to ≈ 1000 Pa) for temperatures ranging from standard to melting conditions (298.15-353.1 K).

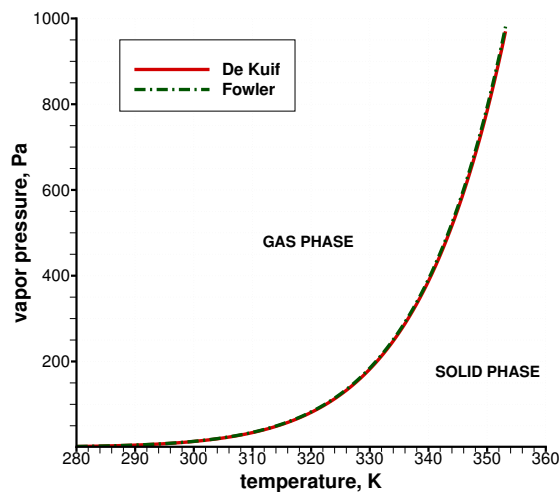


Figure 12: Comparison of different expressions (from Refs. [13] and [11]) for the equilibrium vapor pressure of naphthalene.

NUMERICAL ANALYSIS OF LOW-TEMPERATURE ABLATORS IN A SUPERSONIC WIND-TUNNEL

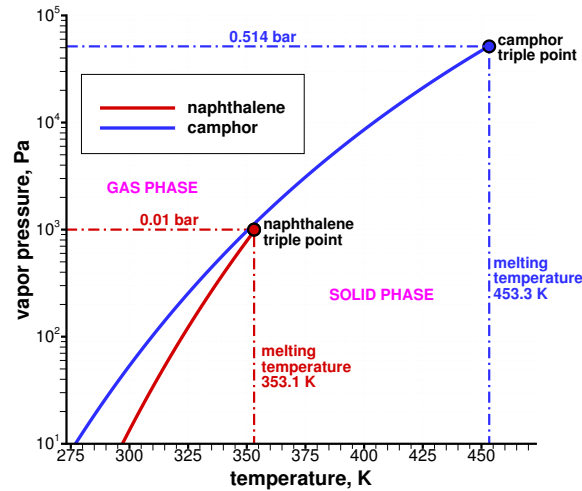
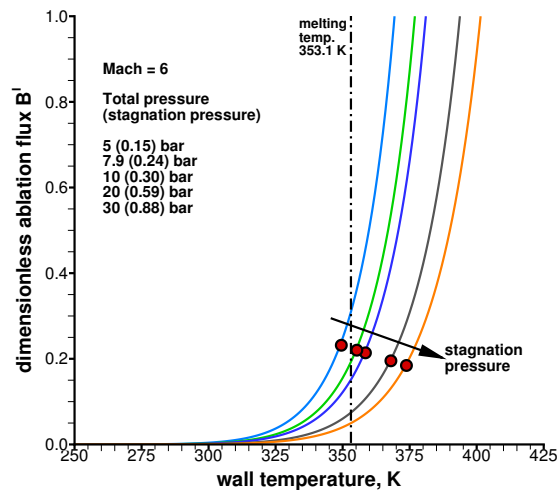


Figure 13: Equilibrium phase diagrams of camphor and naphthalene.

From the knowledge of the vapor pressure and of the atmospheric environment (air), the equilibrium dimensionless sublimation mass flux (B') of naphthalene can be calculated as a function of surface temperature and pressure, as shown in Fig. 14. The curves, calculated at five different pressures corresponding to the stagnation pressure of Phobus capsule at different inflow total pressures ranging from 5 up to 30 bar, show that the blowing rate increases with surface temperature and decreases with pressure. Moreover, the melting temperature could be potentially reached for all of the considered inflow pressures.

Figure 14: Dimensionless ablation mass flux (B') for naphthalene in air as a function of surface temperature (red dots indicate stagnation point conditions from CFD computations).

3.2 Camphor model

Again, the material properties required from the model are: i) the enthalpy of the gaseous sublimating species, ii) the enthalpy of the solid material, and iii) the equilibrium vapor pressure of the sublimating species. These three quantities are needed as a function of temperature.

Camphor is an organic compound with formula $C_{10}H_{16}O$ with a molecular weight of 152.2334. Camphor is a waxy, flammable, white solid. As the CEA database does not include camphor gas, curve fits for camphor gas specific

NUMERICAL ANALYSIS OF LOW-TEMPERATURE ABLATORS IN A SUPERSONIC WIND-TUNNEL

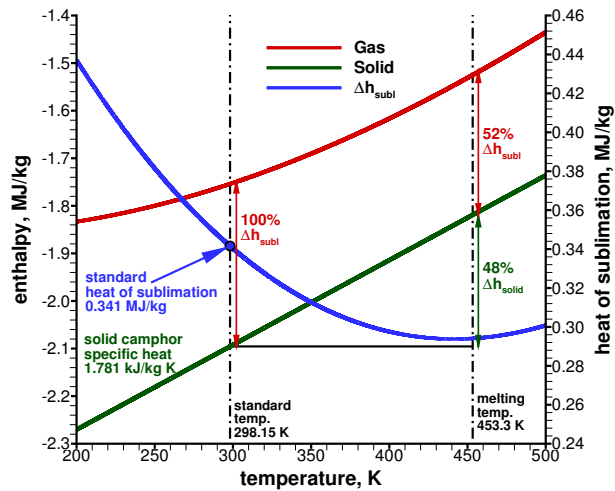


Figure 15: Enthalpy of gaseous and solid camphor and Δh_{subl} as a function of temperature.

heat was modified to have the CEA format and this was added to the database. Solid camphor was represented with a constant specific heat recovered from NIST, as done for naphthalene. Finally, the value of the standard enthalpy of formation of solid camphor is equal to -2.1 MJ/kg. For the transport properties no experimental data have been found and they have been calculated via kinetic theory. Figure 15 shows the camphor gas-phase and solid-phase enthalpies along with the heat of sublimation, $\Delta h_{\text{subl}} = h_c - h_s$, as a function of temperature. The standard heat of sublimation at 298.15 K is 0.341 MJ/kg and the heat of sublimation is decreasing with temperature ranging from standard to melting conditions (298.15 - 453.3 K). Moreover, it is also worth noting that the energy required (per unit of mass) to gasify the solid phase ($\Delta h_{\text{subl}} + \Delta h_{\text{solid}}$) is dominated by the sublimation process, Δh_{subl} , only at low temperatures as the energy required to heat-up the solid, Δh_{solid} , can contribute up to 50% at the highest temperature, i.e. the melting temperature (assuming that the solid is initially at ambient, i.e. standard, conditions). Because of a varying heat of sublimation and of the non-negligible contribution of the solid heating term, the energy required to gasify camphor can change more significantly with temperature in the sublimation regime with respect to naphthalene.

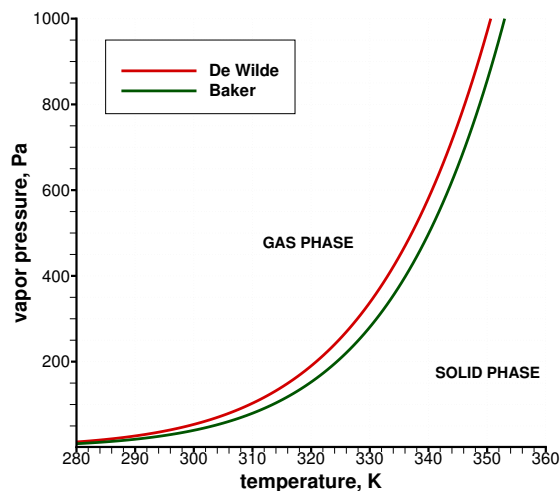


Figure 16: Comparison of different expressions (from Refs. [12] and [1]) for the equilibrium vapor pressure of camphor.

The remaining information to be retrieved is the camphor equilibrium vapor pressure. For the vapor pressure curve of camphor two references have been found, Ref. [12] and [1]. The experimental data retrieved from Ref. [12]

NUMERICAL ANALYSIS OF LOW-TEMPERATURE ABLATORS IN A SUPERSONIC WIND-TUNNEL

have been fitted into an Antoine-like equation

$$p = 10^{A-B/(T+C)} \quad (18)$$

where p [Torr] is the pressure, T [°C] is the temperature and the coefficients A , B and C have been calculated from the experimental data. The procedure followed required the linearization of the Antoine equation expression and the multiple linear regression of the data

$$T \log(P) + C \log(P) = A \cdot T + A \cdot C - B \quad (19)$$

$$\log(P) = A + (A \cdot C - B)/T - C \log(P)/T \quad (20)$$

With this linearization the Antoine equation can be modeled with the following expression

$$y = a_0 + a_1 x_1 + a_2 x_2 \quad (21)$$

where the coefficients correspond to the Antoine equation coefficients A , B and C and the fitted values are respectively

$$\begin{aligned} A &= 8.52 \\ B &= 2714.91 \\ C &= 277.67 \end{aligned}$$

In Fig. 16 both expressions have been plotted in the vapor pressure diagram and compared for a typical range of temperature showing differences of the order of 10 – 20%. Ref. [12] is chosen for the implementation in the CFD code. Note that the effects of using a different expression for the camphor equilibrium vapor pressure in terms of CFD predictions of mass flow rate and wall temperature are very small.

In the phase diagram (Fig. 13) the values of pressure and temperature referring to the triple point are 453.3 K and 51433.14 Pa from Ref. [10]. The vapor pressure of camphor increase by roughly three orders of magnitude (from ≈ 50 to ≈ 50000 Pa) for temperatures ranging from standard to melting conditions (298.15-453.3 K).

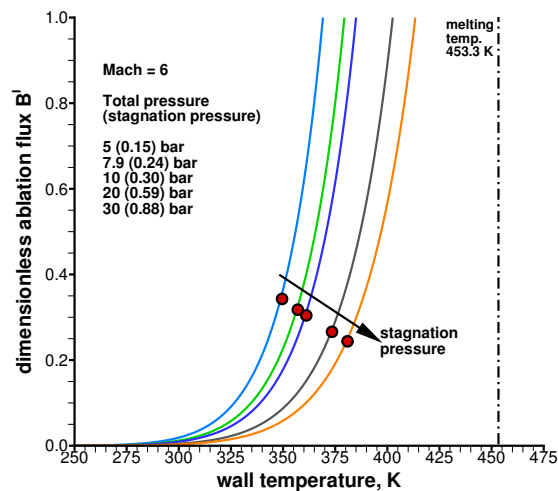


Figure 17: Dimensionless ablation mass flux (B') for camphor in air as a function of surface temperature (red dots indicate stagnation point conditions from CFD computations).

As for naphthalene, the equilibrium dimensionless sublimation mass flux (B -prime) of camphor can be calculated from the knowledge of its vapor pressure and of the atmospheric environment (air) as a function of surface temperature and pressure, as shown in Fig. 17. The curves, calculated at five different pressures corresponding to the stagnation pressure of Phobos capsule at different inflow total pressures ranging from 5 up to 30 bar, show that the blowing rate increases with surface temperature and decreases with stagnation pressure. Moreover, for quite large dimensionless ablation mass fluxes of the order of 1, the melting temperature is far from being reached.

3.3 Comparison of naphthalene and camphor

In order to have a support in the selection of the most suitable low temperature ablator to be used in the H-3 facility, a comparison between naphthalene and camphor major properties are discussed here. First, Fig. 13 shows the equilibrium phase diagrams of camphor and naphthalene in the sublimation/deposition region. The first difference is that camphor is characterized by a higher vapor pressure than naphthalene throughout the entire temperature range. This means that camphor is sublimating at a higher rate than naphthalene at the same temperature. Moreover, camphor has a higher triple point pressure and a higher triple point temperature, hence it is sublimating over a broader temperature range, that is an advantageous characteristic as the melting of the low-temperature ablator is to be avoided. Moreover, the much higher triple point pressure of camphor with respect to naphthalene (0.51 vs 0.01 bar) reduces the occurrence of surface melting for the H-3 wind tunnel operational conditions. In fact, if the maximum pressure of the flow (i.e. the stagnation point pressure) is below the triple point pressure, melting is not possible.

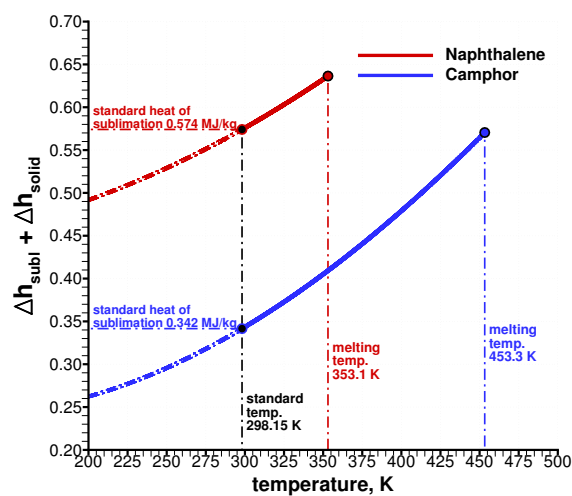


Figure 18: Heat of gasification ($\Delta h_{\text{subl}} + \Delta h_{\text{solid}}$) for naphthalene and camphor as a function of temperature.

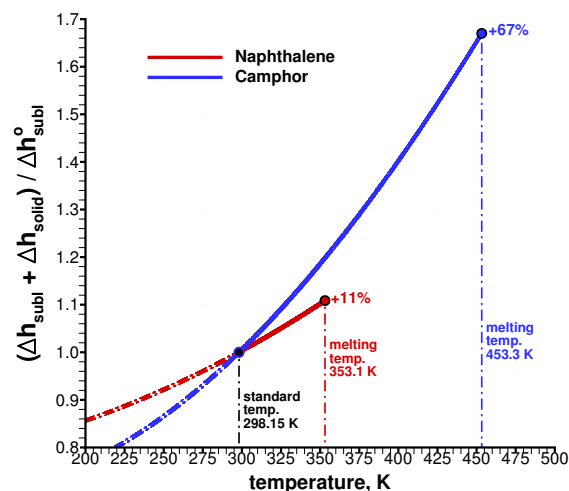


Figure 19: Ratio of heat of gasification over standard heat of sublimation ($\frac{\Delta h_{\text{subl}} + \Delta h_{\text{solid}}}{\Delta h_{\text{subl}}^0}$) for naphthalene and camphor as a function of temperature.

In terms of the amount energy required to gasify the solid material, Fig. 18 shows a comparison between naph-

NUMERICAL ANALYSIS OF LOW-TEMPERATURE ABLATORS IN A SUPERSONIC WIND-TUNNEL

thalene and camphor data assuming that the solid material is at standard conditions (298.15 K). As already discussed, the energy required to gasify naphthalene, $\Delta h_{\text{subl}} + \Delta h_{\text{solid}}$, does not change much in the sublimation regime and ranges from 0.574 to 0.636 MJ/kg for temperatures ranging from standard to melting conditions (298.15-353.1 K). Differently, the energy required to gasify camphor changes more significantly in the sublimation regime and ranges from 0.342 to 0.570 MJ/kg for temperatures ranging from standard to melting conditions (298.15-453.3 K), mainly because of the non-negligible contribution of the solid heating term, Δh_{solid} . This is even more evident by looking at Fig. 19, that shows the ratio of the heat of gasification over the standard heat of sublimation. Obviously this ratio is equal to 1 at standard conditions (298.15 K). While naphthalene heat of gasification is only increasing by roughly 10%, camphor heat of gasification increases by almost 70% for temperatures ranging from standard to melting conditions.

As seen in Fig. 18, the energy required to gasify camphor is only a fraction of the energy required to gasify naphthalene. At ambient temperature (298.15 K) the heat of gasification of camphor is roughly 60% of that of naphthalene while at the melting temperature (353.1 K for naphthalene and 453.3 K for camphor) the heat of gasification of camphor is roughly 90% of that of naphthalene. This is advantageous as it implies a larger ablation mass flux with the same incoming heat flux (that mainly depends on the wind tunnel operational conditions and the capsule shape). Moreover, the fact that the camphor heat of gasification increases significantly with surface temperature (see Fig. 19) is a positive characteristic, as it tends to counteract a further temperature increase as the temperature approaches the melting temperature. Again, this is an advantageous characteristic as the melting of the low-temperature ablator is to be avoided.

Finally, the density of naphthalene is 1140 kg/m³ and the density of camphor is 990 kg/m³ which, according to Eq. (2), yields a 15% higher recession rate for the less dense camphor at the same mass blowing flux. In conclusion, camphor is deemed more suitable than naphthalene to the current goal of inducing capsule shape change of a low-temperature ablator in a low-enthalpy hypersonic wind tunnel for the following main reasons: i) it has a higher melting temperature and a higher triple point pressure, ii) it has a higher vapor pressure, iii) it has a lower heat of gasification, and iv) it has a lower density. Those characteristics ensure a higher recession rate with a reduced risk of triggering surface melting. This latter aspect is also helped by the significant increase of the camphor heat of gasification with increasing surface temperature. Moreover, for wind tunnel operational conditions that do not provide a wall pressure higher than 0.51 bar (the camphor triple point pressure), melting is not possible. Considering the normal shock relations, this condition translates into a total pressure of roughly 17 bar. For naphthalene, on the other hand, the same condition (considering the naphthalene triple point pressure of 0.01 bar) translates into a total pressure of less than 1 bar. Hence naphthalene can potentially melt throughout the entire total pressure range of the H-3 facility (provided that the heat flux is high enough), while camphor can not melt for total pressures below 17 bar (regardless of the heat flux).

4. Coupling between Aerothermodynamics, Ablation and Shape-Change

The hypersonic and aerothermal problem under scrutiny include coupling between the fluid motion, aerothermal effects, surface boundary conditions, and the material thermal response. When the surface thermodynamic state is such to activate ablation, the surface is also recessing (with a recession rate that is changing over space), causing geometric shape change (which induces a recession rate variation over time). The developed CFD code may be run in a mode to model all these effects in a coupled fashion. In this section, simulations of low-temperature ablators (naphthalene and camphor) undergoing sublimation, internal heating and shape change under H-3 hypersonic wind tunnel operational conditions are analyzed for the scaled-down Phoebe capsule. A validation test case is also reported and analyzed. Before discussing the computed simulations, the mesh generation and mesh evolution procedure is first presented. In general, in a shock-capturing solution of a hypersonic flow, the shock capture represents one of the most important source of numerical error that can negatively affects the quality of overall solution. In fact, it is well known in the CFD community that the numerical simulation of hypersonic flows past blunt bodies by means of classical shock-capturing solvers shows sometimes specific drawbacks and nasty surprises caused by the numerical capture process of the shocks, i.e., stagnation point anomalies, carbuncle phenomenon, and, more generally, low solution quality. This situation is exacerbated by the tendency of an initially sphere-cone configuration to become more blunt when the flow over the nose is all laminar, such is the case for H-3 facility. As the nose gets more blunt, the carbuncle phenomena and the associated stagnation point anomalies can worsen up to a point that the capsule shape can not be evolved anymore in time as the CFD solution is too deteriorated. To reduce these drawbacks due to the capture process and to improve the solution without increasing the number of grid cells, quality specific treatments of strong shocks have to be performed. For this activity, a specific computing procedure based on a mesh-adaptation strategy that ensures a high solution quality has been developed. The key elements of this procedure are: i) a mesh topology that is suitable to manage the cell clustering in the critical regions (e.g. the shoulder region and the sphere-cone junction), and ii) a mesh adapting procedure for the shock regions. Starting from the initial capsule shape, a non-adapted structured

NUMERICAL ANALYSIS OF LOW-TEMPERATURE ABLATORS IN A SUPERSONIC WIND-TUNNEL

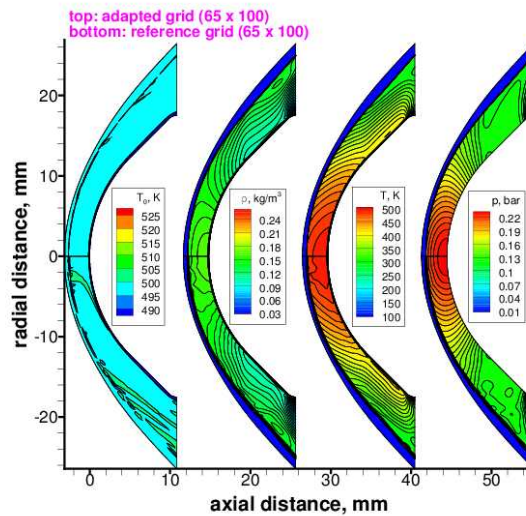


Figure 20: Non-adapted mesh and adapted mesh solution quality in terms of total temperature, density, static temperature and pressure flowfields (from left to right).

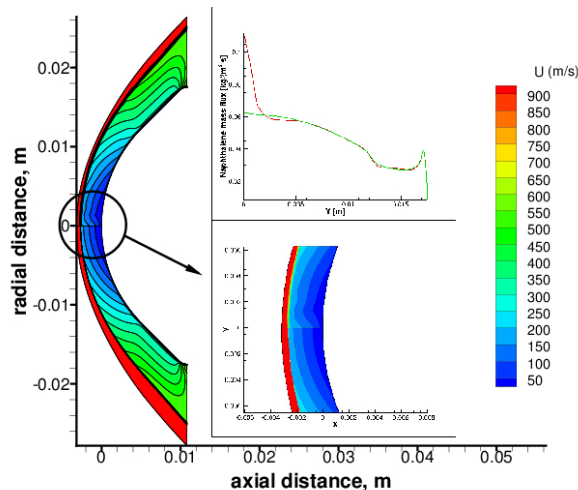


Figure 21: Non-adapted mesh (top, red) and adapted mesh (bottom, green) solution quality in terms of axial velocity flowfield and sublimation mass flux distribution.

mesh is generated. The numerical solutions, computed on the non-adapted meshes, are then post-processed in order to adapt and refine the mesh in the shock regions and reduce the negative effects caused by the numerical shock capture. Lastly, the final solutions are obtained by the re-computation on the adapted meshes. An example of this process is shown in Figs. 20 and 21. The carbuncle effect is clearly visible around the stagnation point in terms of a “depression” of the velocity isolines in the flow field, as shown in Fig. 21. Furthermore, the same figure shows the behavior of the sublimating naphthalene mass flux at the surface as a function of the radial coordinate of the model shape. The mass flux near the stagnation point is completely distorted by the carbuncle phenomena resulting in a non-physical and relevant increase of the sublimation flux in that region. This effect is intensified when cells are elongated in the direction normal to the shock, that is also a side effect of the recession process. In fact, when the profile consumption is propagated in time to simulate the ablation phenomenon, as the body tends to flatten in the stagnation region, the shock distance increases, decreasing the cell aspect ratio in the direction tangent to the shock. Moreover, because of surface recession, the distance between the profile points decreases leading to more elongated cells in the direction normal to the shock. These aspects would require a continuous increase in the number of cells in the direction normal to the shock to dampen the increasing carbuncle effect, thus leading to high computational time as the body surface is

NUMERICAL ANALYSIS OF LOW-TEMPERATURE ABLATORS IN A SUPERSONIC WIND-TUNNEL

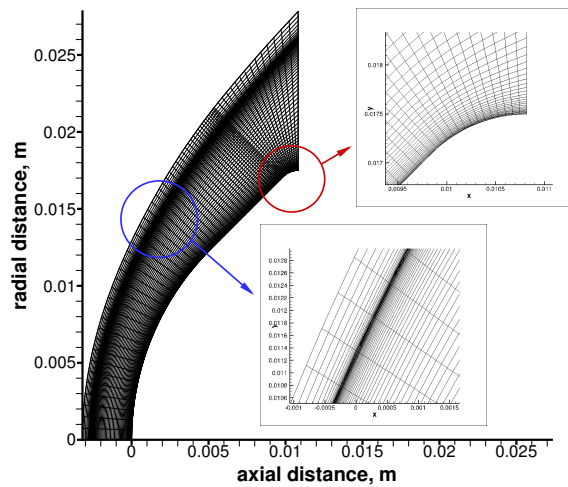


Figure 22: Details of the adapted mesh.

recessed. For this reason, a solution based on mesh adaptation techniques is adopted that improve the efficiency of the solution both in terms of computational cost and shock-layer resolution. The mesh adapting procedure takes effect only on regions where strong shocks are present. Therefore, the procedure does not alter in significant way the original cell distribution inside the boundary layer, so that wall gradient resolution is retained. Indeed, only the mesh nodes of the shock layer outer region and those outside the shock layer are moved toward the shocks, as shown in Fig. 22, without increasing the total number of nodes. The effect of the adaptive mesh refinement is evident not only on the flowfield (see Fig. 20) but also on the surface fluxes, such as the ablation mass flux due to sublimation (see Fig. 21). Once

Mach	Static Temperature	Static Pressure	Total Pressure
6	61 K	320 Pa	5 bar
6	61 K	500 Pa	7.9 bar
6	61 K	633 Pa	10 bar
6	61 K	1266 Pa	20 bar
6	61 K	1899 Pa	30 bar

Table 1: Inflow conditions for camphor and naphthalene numerical tests.

the mesh generation procedure has been set-up, numerical simulations of camphor and naphthalene sublimation under various inflow conditions of the H-3 wind tunnel facility are computed. Table 1 shows the different inflow conditions that are used.

Figure 23 shows the axial distributions of sublimation mass flux, wall temperature, wall convective heat flux and wall pressure for camphor at the five different wind tunnel inflow total pressures. The sublimation mass flux can be increased by almost two times by increasing the inflow total pressure from 5 up to 30 bar although, as we have seen, the dimensionless sublimation mass flux $B\text{-prime}$ is actually decreasing and the blowing effect gets less intense. The maximum value of the ablation mass flux is at the stagnation point but there is a local maximum also in the shoulder region, due to the rapid expansion that accelerates the flow and increases the heat transfer locally. The maximum wall temperature (see Fig. 23(b)) is at the stagnation point and ranges from 350 up to 380 K for a inflow total pressure of 5 and 30 bar, respectively. The wall temperature is always well below the melting temperature of camphor (453.3 K).

Figure 24 shows the axial distributions of sublimation mass flux, wall temperature, wall convective heat flux and wall pressure for naphthalene at different wind tunnel total pressures (ranging from 5 up to 30 bar). As for camphor, the sublimation mass flux of naphthalene can be increased by almost two times by increasing the inflow total pressure from 5 up to 30 bar. However, the maximum value of the ablation mass flux is roughly 25% lower than the corresponding value for camphor. Hence, numerical results are confirming that the sublimation rate of camphor is higher with respect to that of naphthalene at the same wind tunnel operational conditions. The maximum wall temperature (see Fig. 24(b)) for naphthalene can exceed the maximum allowable temperature (i.e. the melting temperature 353.1 K) for four cases

NUMERICAL ANALYSIS OF LOW-TEMPERATURE ABLATORS IN A SUPERSONIC WIND-TUNNEL

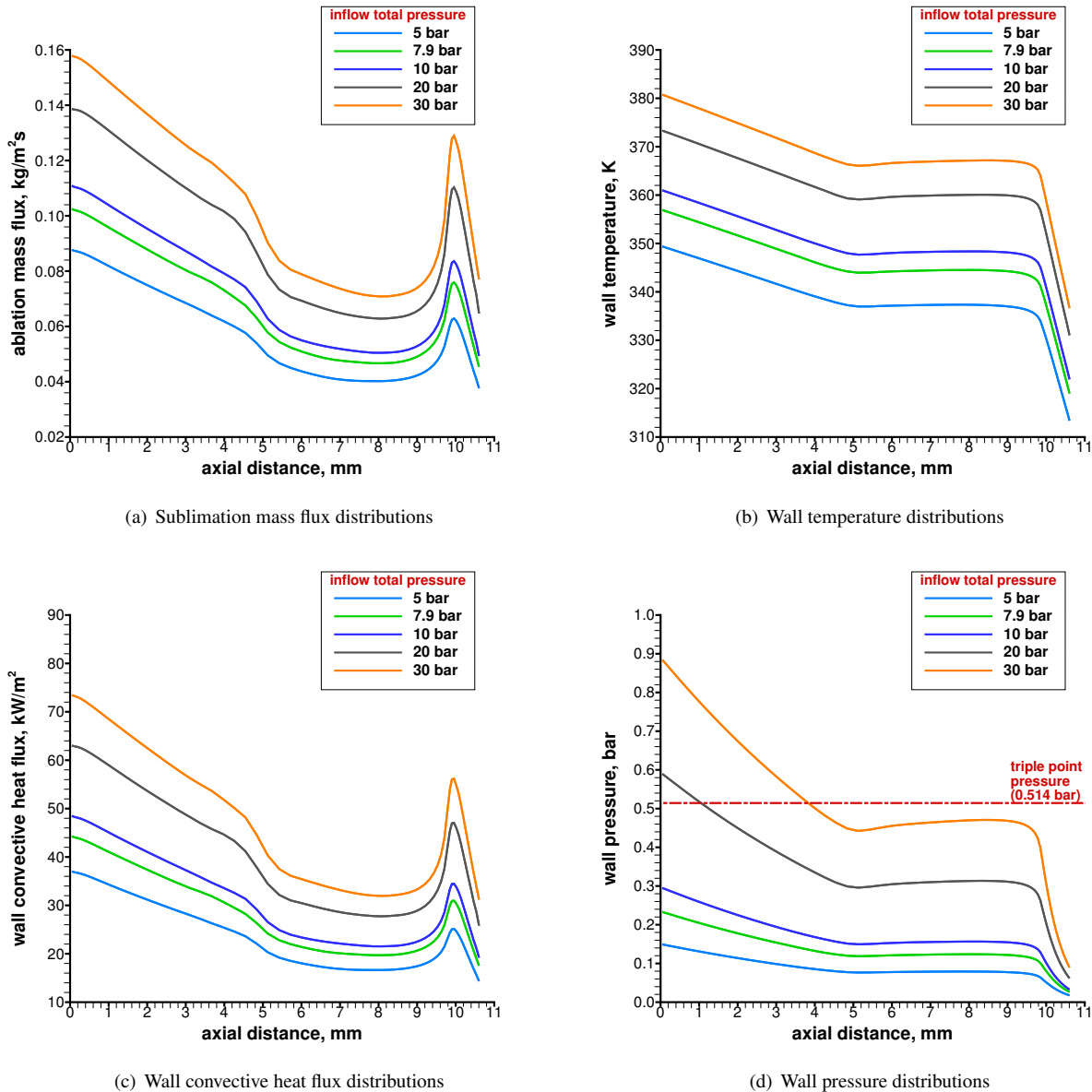


Figure 23: Camphor distributions for the five selected inflow total pressures.

out of five, at the higher inflow total pressures (e.g. 7.9, 10, 20, and 30 bar). Only for the lowest inflow total pressure of 5 bar the wall temperature is everywhere below the melting temperature. Surface melting is confirmed by several experimental tests performed in H-3 starting from a total pressure of the order of 10 bar, as predicted by the numerical solutions. Figure 25 shows the distribution of the sublimating gas partial pressure with respect to temperature throughout the entire flowfield. Results show that, due to the sudden expansion in the shoulder region, the partial pressure of the sublimating gas, for both camphor and naphthalene cases, can rise above the local vapor pressure which means that the deposition process (i.e. the reverse of sublimation) is favored. This condition is only reached in the shoulder region for all of the considered inflow total pressures, and the effect gets stronger as the inflow total pressure is increased. A confirmation of this phenomenon is found in experimental tests, that show streaks of solid naphthalene depositing on the surface at the rear edge of the capsule. As shown in Fig. 25(a), on the other hand, the appearance of liquid camphor is never occurring. Differently, for naphthalene cases shown in Fig. 25(b), there is the occurrence of the liquid phase near the stagnation point region at the higher considered inflow total pressures. Again, naphthalene surface melting is confirmed by several H-3 tests.

NUMERICAL ANALYSIS OF LOW-TEMPERATURE ABLATORS IN A SUPERSONIC WIND-TUNNEL

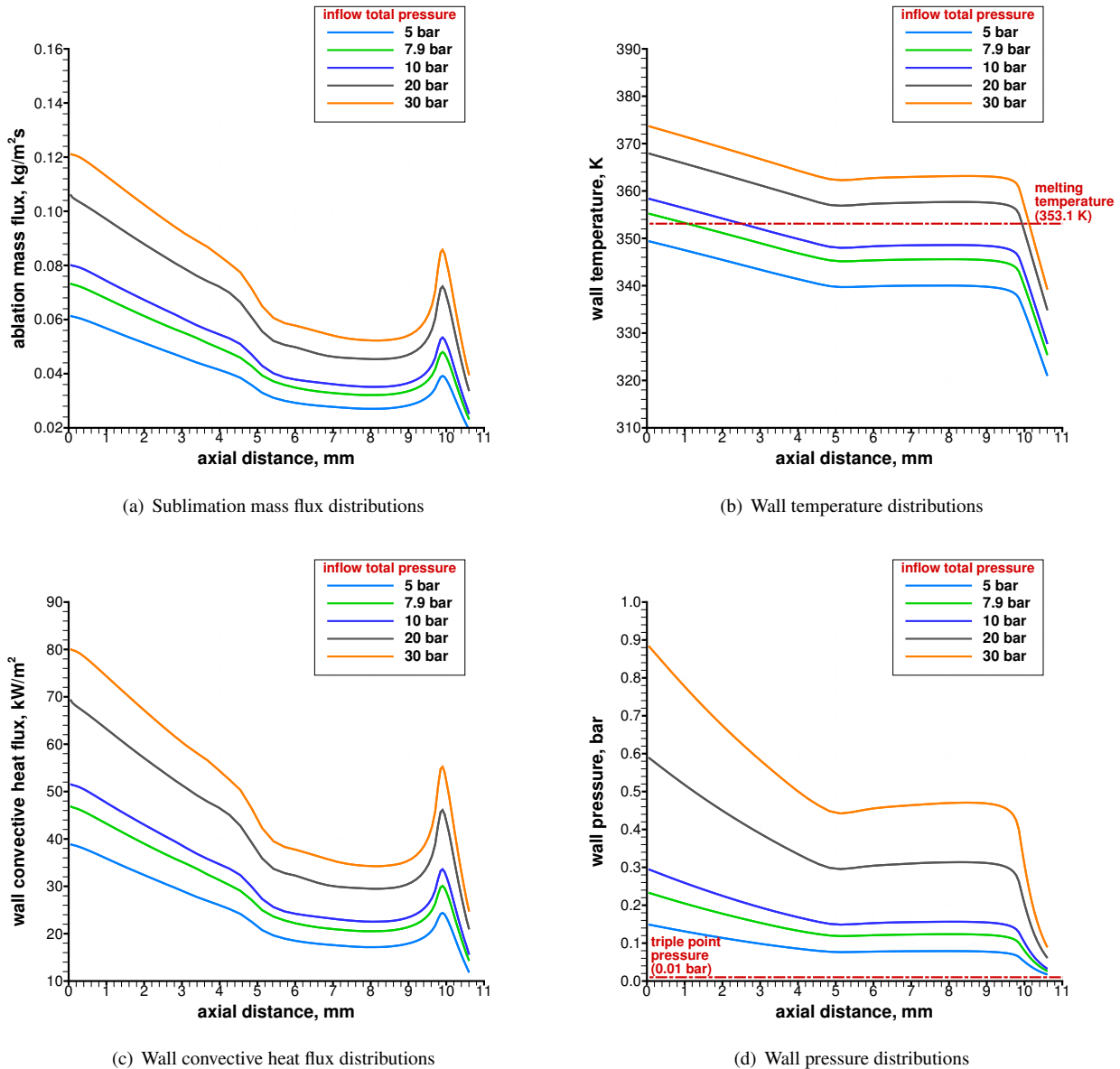


Figure 24: Naphthalene distributions for the five selected inflow total pressures.

5. Model validation including shape change

In order to show the capability of the present approach to predict the capsule shape change due to coupling between the surface ablation and the aerothermodynamic environment, a more complete validation test case has been performed. To this goal, experiments conducted by Baker¹ were used to validate the camphor boundary condition. The Baker experiments studied camphor models in both a laminar and turbulent environment. Here we focus on an axisymmetric case, for which the flow is laminar and the time-dependent geometry profile data are available. The initial shape of the model is a spherically-blunted cone with a 6.35 cm nose radius, 8° half-angle cone, 23.88 cm in length and the wind tunnel freestream conditions are $\rho = 0.04 \text{ kg/m}^3$, $T = 132 \text{ K}$, $U = 1155 \text{ m/s}$ and freestream unit Reynolds number of $5 \times 10^6 / \text{m}$. These freestream conditions correspond to $M = 5.0$, $p_0 = 8.07 \text{ bar}$, and $T_0 = 797 \text{ K}$. These conditions produce a fully laminar flow environment. The test was conducted for more than 5 minutes and pre-test and post-test photographs are shown in Fig. 26. The CFD code was used to perform fully-coupled simulations of camphor sublimation, thermal response (assuming steady-state ablation), and shape change. The total exposure time of the model is 320 seconds. Shape change simulations have been performed up to a total elapsed exposure time of 200 seconds. After 200 seconds the solid recessed a considerable amount, equivalent to roughly 50% of the initial nose radius, that would require the grid topology to be changed in order to proceed with further shape change. However,

NUMERICAL ANALYSIS OF LOW-TEMPERATURE ABLATORS IN A SUPERSONIC WIND-TUNNEL

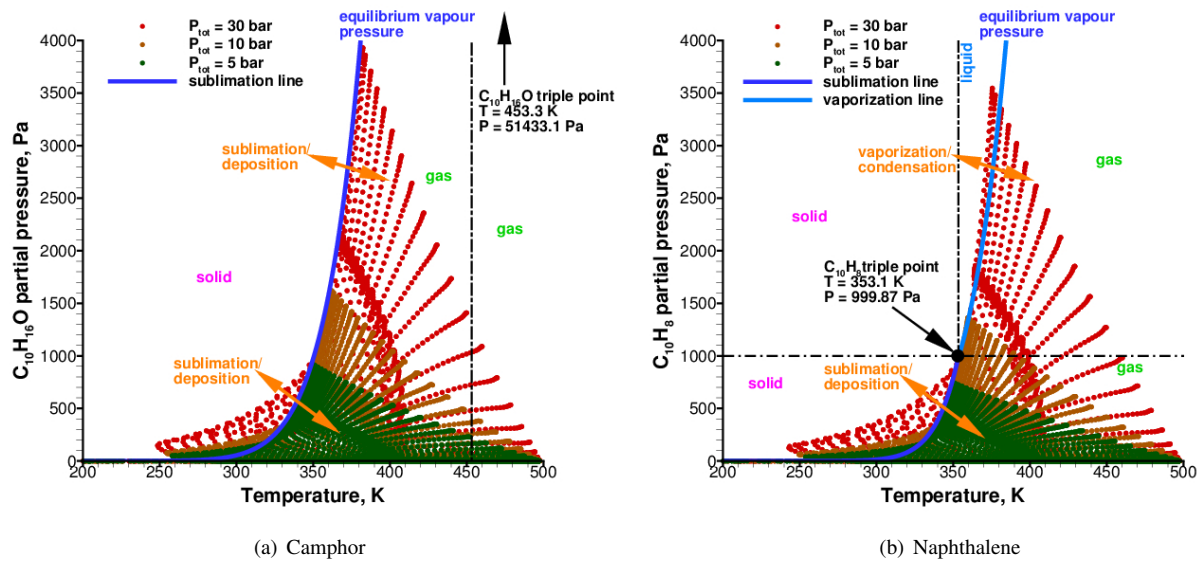


Figure 25: Map of sublimating species partial pressure vs temperature throughout the entire flowfield for three inflow total pressures (5, 10, and 30 bar).

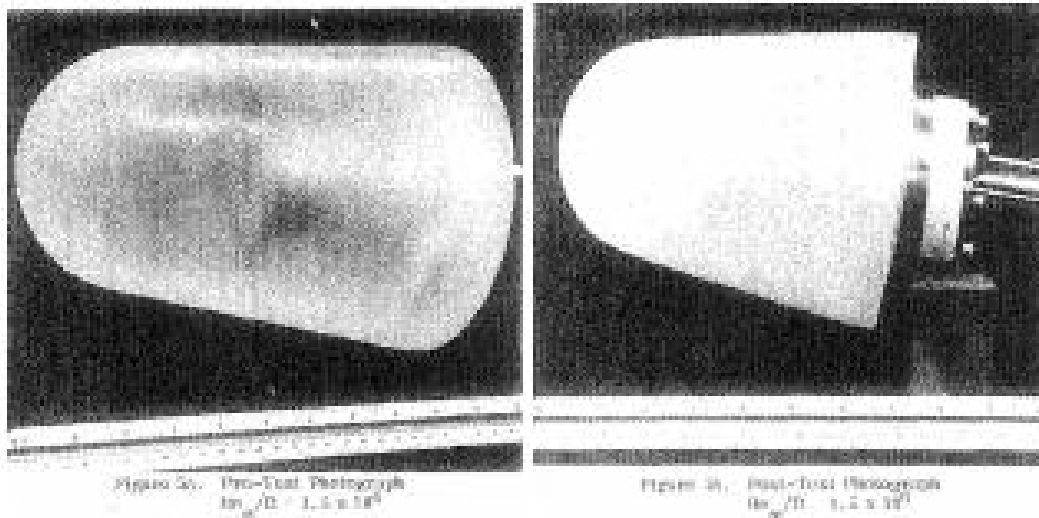


Figure 26: Test photographs before (left) and after (right) the test from the Baker experiments.¹

for the current purposes of validation this was not deemed necessary and the predicted recessed shape is compared to the experimentally measured one at two different time instant, 80 and 200 seconds. It is worth mentioning that these exposure times are both larger than what is allowable in the H-3 facility, with the freestream conditions being very similar. Hence this test is perfectly suitable to our goals.

Figure 27 shows the pressure and temperature contours at the initial time and after 200 seconds of exposure. The significant amount of recession is also evident from the plots. Figure 28 compares the flowfield around the model at the first and last time step (the final profile at 200 seconds has been shifted in order to have the same initial position of the initial profile). Firstly, it can be noticed that the geometry profile of the model at 200 seconds is flatter than the initial one thus leading to an increased curvature radius and a lower heat flux and, consequently, a lower recession rate. Finally, the flattening of the body induces an increase in the shock stand-off distance and in the bow shock angle in the conical region. Figure 28 also shows the sublimation mass flux distribution along the surface at the initial time and at the final time, highlighting the shape change effect. Increasing the exposure time, the sublimation mass flux is reduced in the stagnation region and in the sphere-cone junction while it is increased in the conical region. Comparisons between the shape change of the ablation boundary condition are also shown in Fig. 29 at 0 seconds, 80 seconds, and

NUMERICAL ANALYSIS OF LOW-TEMPERATURE ABLATORS IN A SUPERSONIC WIND-TUNNEL

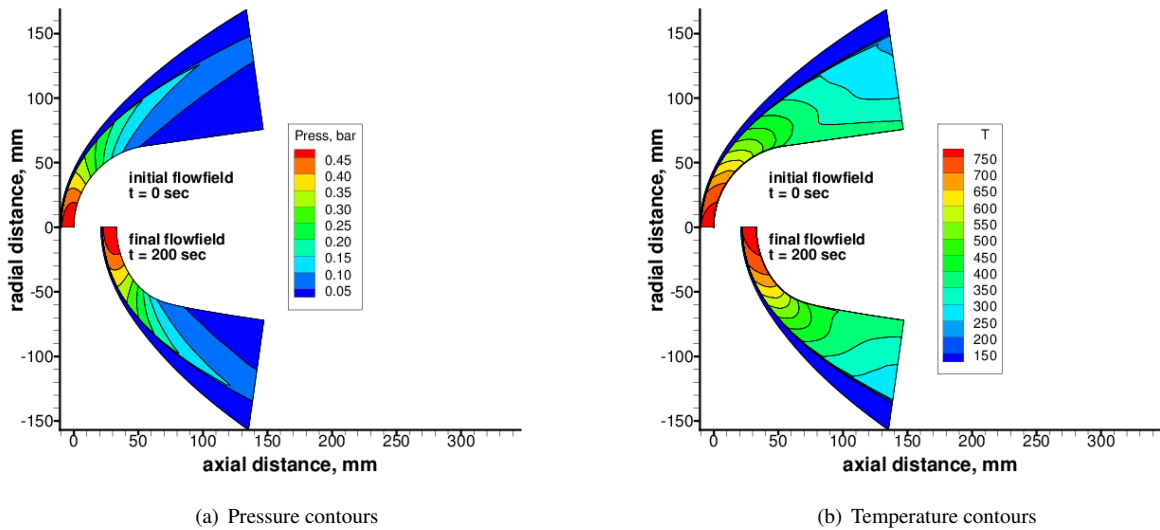


Figure 27: Pressure and temperature contours at 0 and 200 seconds of exposure.

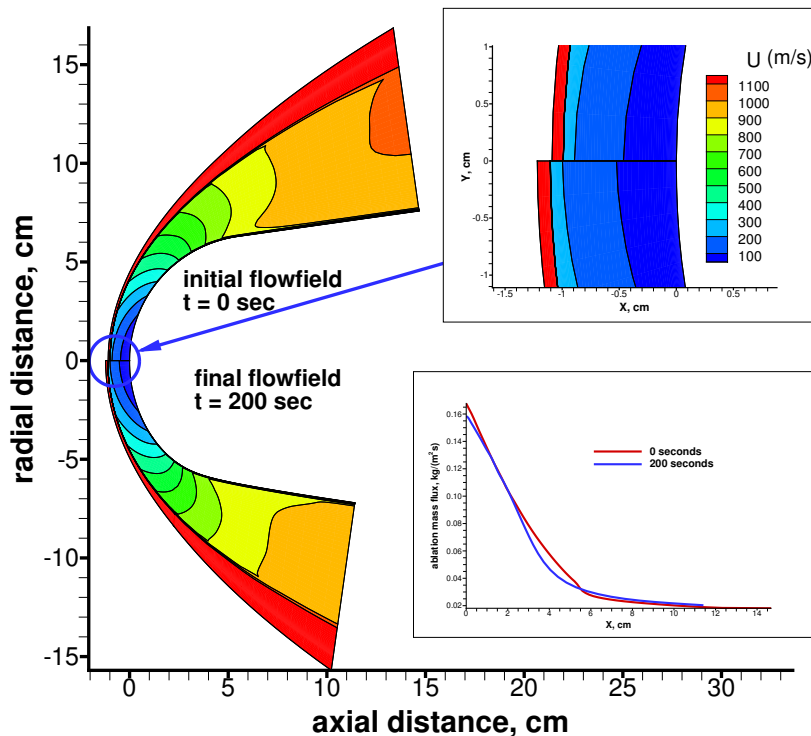


Figure 28: Axial velocity contours (with details of shock stand-off distance) and sublimation mass flux distributions at 0 and 200 seconds of exposure.

160 seconds for different time steps between subsequent CFD simulations. With a time step of 80 s, 3 CFD simulations are performed from zero to 160 seconds. With a time step of 40 s, 5 CFD simulations are performed. With a time step of 10 s, finally, 17 CFD simulations are performed. Results show a clear convergence as the time step between subsequent simulations is reduced. In particular, the sphere-cone junction and the shoulder are more sensitive to the shape change effect than the stagnation point. A time step of 10 s is considered sufficiently refined to get an accurate evolution of

NUMERICAL ANALYSIS OF LOW-TEMPERATURE ABLATORS IN A SUPERSONIC WIND-TUNNEL

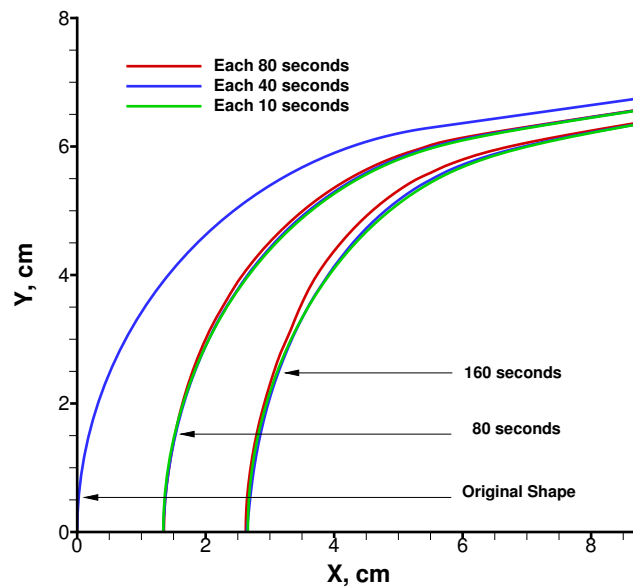


Figure 29: Comparison of the model shape at different times with different time steps between subsequent CFD simulations (80, 40, and 10 s).

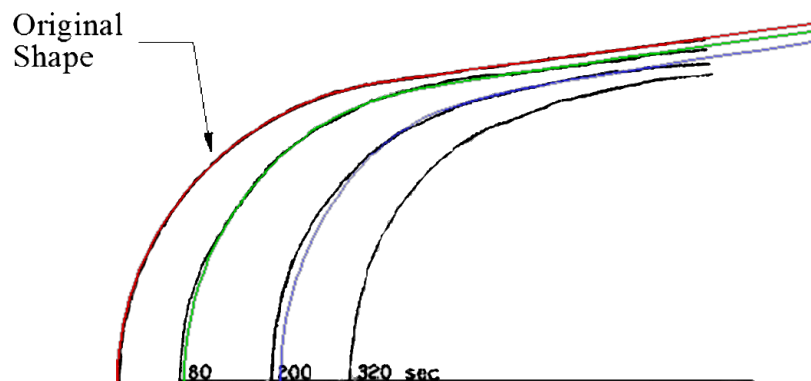


Figure 30: Comparison between the model shape from experimental data (black lines) and from simulations at different times.

the model shape. Finally, the comparison between the predicted shape (with a time step of 10 s) and the experimental one is shown in Fig. 30 at 0 seconds (red), 80 seconds (green), and 200 (blue) seconds. Both the stagnation point and side wall recession are in very good agreement with the experimental data. The comparison is very favorable, with the stagnation point recession captured with an error of less than 5% (overestimation), as well as the variation with time of the entire profile. It is worth mentioning that the solid camphor initial temperature is assumed to be 298.15 K, although the actual experimental value is not given. With a stagnation point temperature of 390 K, the corresponding heat of gasification would be of 0.46 MJ/kg. If the solid camphor initial temperature was assumed 290 K instead of 298.15 K, the heat of gasification would increase by $\approx 3\%$. At 280 K initial temperature, the camphor heat of gasification would

NUMERICAL ANALYSIS OF LOW-TEMPERATURE ABLATORS IN A SUPERSONIC WIND-TUNNEL

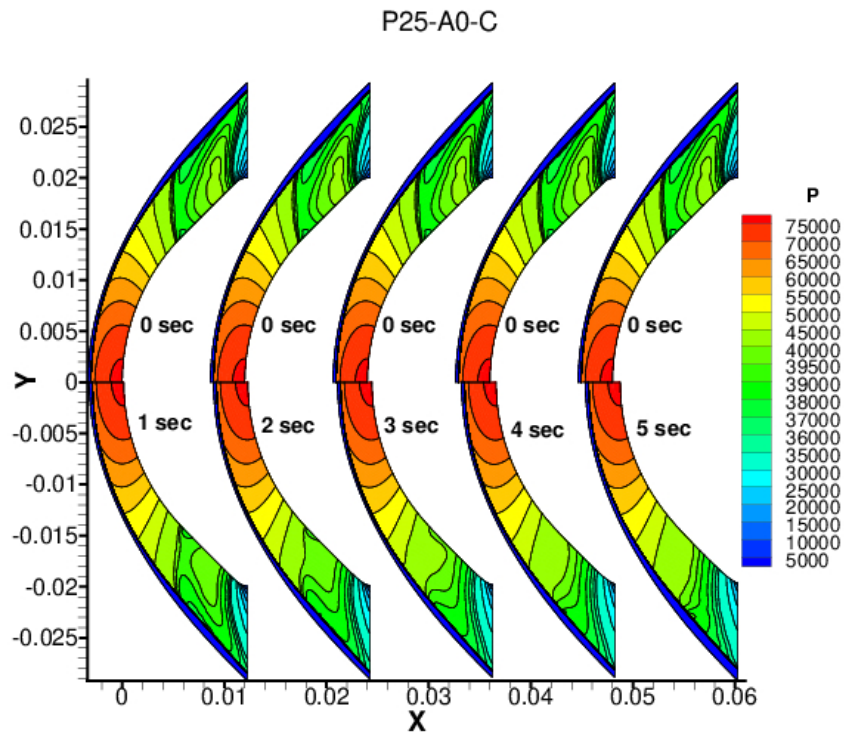


Figure 31: Pressure contour for the Phoebus capsule at several times.

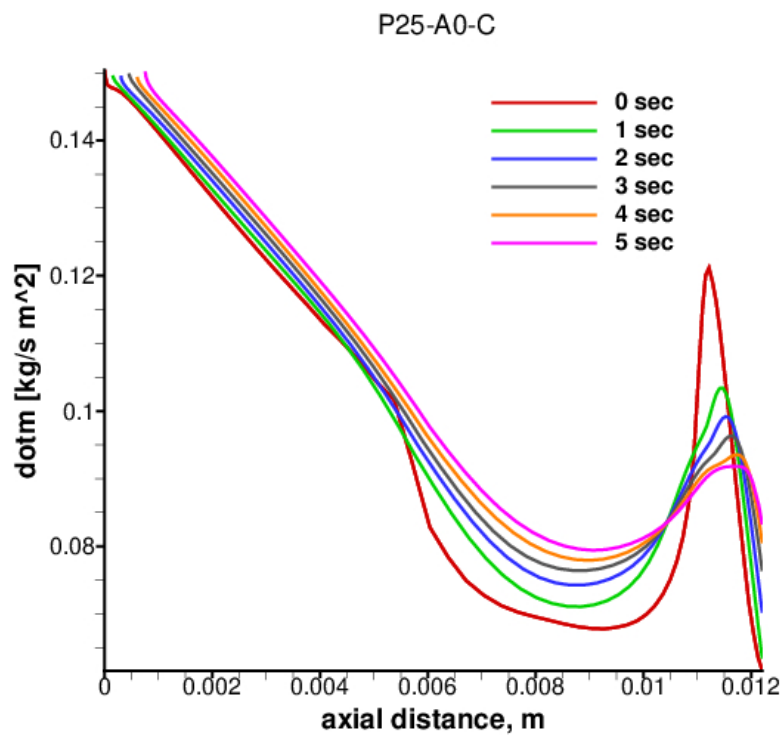


Figure 32: Sublimation mass flux distributions for the Phoebus capsule at several times.

increase by $\approx 7\%$. Hence, the small overestimation of stagnation point recession can be reduced to almost zero if the

NUMERICAL ANALYSIS OF LOW-TEMPERATURE ABLATORS IN A SUPERSONIC WIND-TUNNEL

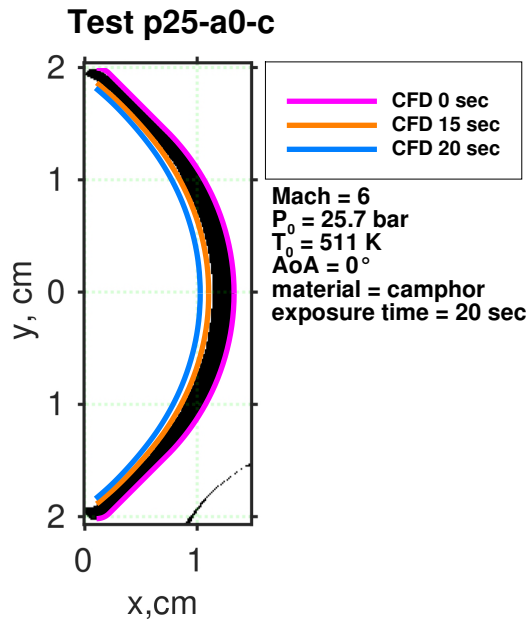


Figure 33: Comparison of Phoebus capsule shape after 20 sec of exposure: measured (black) vs computed (blue).

solid camphor initial temperature is assumed to be in the range 285-290 K. As this information is not available from the experiments, there is a certain level of uncertainty ($\pm 5\%$).

Finally, Fig. 31 shows the pressure contour for the Phoebus capsule in H-3 during the first 5 sec of exposure. Figure 32 shows the sublimation mass flux distributions for the Phoebus capsule during the same time. It is worth noting that shape change effects are more evident in the first few seconds of exposure. In particular this appears to be due to the sphere-cone junction and the spherical shoulder that, after a few seconds of exposure, are smoothed by the ablation process. As shown in Fig. 32, after roughly 5 seconds of exposure, the ablation mass flux profile along the wall is significantly smoother with respect to the initial value. This smoothing between the pre-ablation shape and the post-ablation shape is also evident by looking at pressure isolines in Fig. 31. Finally, the comparison between the predicted shape and the experimental one is shown in Fig. 33 after 20 seconds of exposure. Both the stagnation point and side wall recession are in fair agreement with the experimental data, although the CFD prediction is overestimating the surface recession (a better agreement is found with the CFD predicted shape after 15 seconds). Such an underestimation could be explained by the lacking of a transient heating in the solution, as CFD results are assumed to reach instantaneously the steady-state condition. It is worth noting that this discrepancy was much less evident for the Baker experiment, as the exposure time was 10 times larger than the H-3 one. A much longer exposure time makes the initial heating transient more negligible.

6. Conclusions

A preliminary capsule shape sensitivity analysis has been performed that resulted in the selection of a Phoebus-like scaled-down capsule. The Phoebus-like capsule, in fact, appeared to be the best solution in terms of pressure and heat flux distributions along the surface with a pronounced wall pressure variation in the first half of the capsule, that is expected to produce a visible shape change effect. Hence, the Phoebus capsule appears to be the best trade-off in terms of volume available for the instrumentation of balances, reduced bow-shock angle for stable wind tunnel operations, and non-uniform pressure and heat flux distributions along the surface to highlight shape change effects. An overview of the two selected low-temperature ablators behavior in H-3 wind tunnel conditions was given. The several benefits of using camphor with respect to naphthalene have been highlighted. More specifically, camphor is deemed more suitable than naphthalene to the current goal of inducing capsule shape change of a low-temperature ablator in a low-enthalpy hypersonic wind tunnel for the following main reasons: i) it has a higher melting temperature and a higher triple point pressure, ii) it has a higher vapor pressure, iii) it has a lower heat of gasification, and iv) it has a lower density. Those characteristics ensure a higher recession rate with a reduced risk of triggering surface melting. This latter aspect is also helped by the significant increase of the camphor heat of gasification with increasing surface temperature. Moreover, for wind tunnel operational conditions that do not provide a wall pressure higher than 0.51 bar (the camphor triple point pressure), melting is physically not possible. The camphor model introduced in the CFD code has been validated through comparison with experimental data obtained from wind tunnel tests of a spherically-blunted cone camphor model exposed to a high-speed flow for several minutes and producing a significant shape change with more than 50% of nose recession relative to its radius. The mesh generation and mesh evolution procedure has been presented and discussed. In particular, it is shown that the carbuncle phenomena and the associated stagnation point anomalies can worsen up to a point that the capsule shape can not be evolved anymore in time as the CFD solution is too deteriorated. To reduce these drawbacks due to the capture process and to improve the solution without increasing the number of grid cells, a specific computing procedure based on a mesh-adaptation strategy that ensures a high solution quality has been developed.

Acknowledgments

This work has been supported and funded by ESA-ESTEC under ESA TRP contract no. 4000121241/17/NL/KML *Modelling Capsule Stability Accounting for Shape Change - EXPRO PLUS* with the von Karman Institute for Fluid Dynamics as prime contractor.

References

- [1] R. L. Baker. Low temperature ablator nosetip shape change at angle of attack. *10th Aerospace Sciences Meeting*, (1972-90), 1972.
- [2] D. Bianchi and F. Nasuti. Numerical analysis of nozzle material thermochemical erosion in hybrid rocket engines. *Journal of Propulsion and Power*, 29(3):547–558, 2013. doi: 10.2514/1.B34813.
- [3] D. Bianchi, F. Nasuti, and E. Martelli. Navier-stokes simulations of hypersonic flows with coupled graphite ablation. *Journal of Spacecraft and Rockets*, 47(4):554–562, 2010. doi: 10.2514/1.47995.
- [4] D. Bianchi, F. Nasuti, and M. Onofri. Aerothermodynamic analysis of reentry flows with coupled ablation. AIAA Paper 2011-2273, 2011. doi: 10.2514/6.2011-2273.
- [5] D. Bianchi, F. Nasuti, M. Onofri, and E. Martelli. Thermochemical erosion analysis for graphite/carbon-carbon rocket nozzles. *Journal of Propulsion and Power*, 27(1):197–205, 2011. doi: 10.2514/1.47754.
- [6] D. Bianchi, F. Nasuti, R. Paciorri, and M. Onofri. Computational analysis of hypersonic flows including finite rate ablation thermochemistry. In Proc. 7th European Workshop on Thermal Protection Systems and Hot Structures, April 2013, ESA SP-. Noordwijk, The Netherlands, ESA-ESTEC.
- [7] D. Bianchi, F. Nasuti, R. Paciorri, and M. Onofri. Hypersonic flow analysis including finite rate ablation thermochemistry. 5th European Conference for Aeronautics and Space Sciences, Munich, Germany, 1-5 July 2013.
- [8] D. Bianchi, A. Turchi, F. Nasuti, and M. Onofri. Chemical erosion of carbon-phenolic rocket nozzles with finite-rate surface chemistry. *Journal of Propulsion and Power*, 29(5):1220–1230, 2013. doi: 10.2514/1.B34791.

NUMERICAL ANALYSIS OF LOW-TEMPERATURE ABLATORS IN A SUPERSONIC WIND-TUNNEL

- [9] A. F. Charwat. Exploratory studies on the sublimation of slender camphor and naphthalene models in a supersonic wind-tunnel. Advanced Research Project Agency, Memorandum RM-5506-ARPA, 1968.
- [10] A. F. Charwat. Exploratory studies on the sublimation of slender camphor and naphthalene models in a supersonic wind-tunnel. *Advanced Research Project Agency, Memorandum RM-5506-ARPA*, 1968.
- [11] C. G. De Kruif, T. Kuipers, J. C. Van Miltenburg, R. C. F. Schaake, and G. Stevens. The vapour pressure of solid and liquid naphthalene. *The Journal of Chemical Thermodynamics*, 13(11), 1981.
- [12] J. H. De Wilde. *Über die dampfdrucke des kampfers*. 1937.
- [13] L. Fowler, W. N. Trump, and C. E. Vogler. Vapor pressure of naphthalene: New measurements between 40° and 180°c. *Journal of Chemical & Engineering Data*, 13(2), 1968.
- [14] T. K. Sherwood and C. Johannes. The maximum rate of sublimation of solids. *A.I.Ch.E. Journal*, 8(5), 1962.
- [15] A. Turchi, D. Bianchi, F. Nasuti, and M. Onofri. A numerical approach for the study of the gas-surface interaction in carbon-phenolic solid rocket nozzles. *Aerospace Science and Technology*, 27(1):25–31, 2013. 10.1016/j.ast.2012.06.003.